

# Sensorless Control Strategy for Switched Reluctance Traction Drive Based on High Frequency Injection



Pavel Sovicka, Giacomo Scelba, Pavol Rafajdus, and Vladimir Vavrus

**Abstract** This paper deals with the implementation of a sensorless control strategy devoted to Switched Reluctance Motor Drives used in the traction drive of a small truck. The sensorless technique operates at low and zero speed. In the proposed approach an additional high frequency magnetic field is injected into the machine and a suitable demodulation algorithm is exploited to extract useful information on the rotor position and speed. The feasibility of the implementation is verified by simulations.

## 1 Introduction

The anticipated proliferation of electric vehicles in upcoming years leads to a development focused on electric traction drives. Thanks to its inherent robustness, simplicity, and low manufacturing cost the Switched Reluctance Motor (SRM) is a perspective machine. For efficient operation it requires a suitable converter and accurate position information [1, 2]. An example of this focus can be seen in [3, 4]. To increase reliability and fault-tolerance, the position sensor must be backed up by a sensorless alternative. This paper focuses on a development and simulation analysis of a new sensorless method for low speed and low load operating conditions. For high speed and high load torque conditions other methods have to be used, e.g., [5–7].

---

P. Sovicka (✉) · P. Rafajdus · V. Vavrus  
KVES – University of Zilina, Univerzitna 8215/1, Zilina, Slovakia  
e-mail: [pavel.sovicka@fel.uniza.sk](mailto:pavel.sovicka@fel.uniza.sk); [pavol.rafajdus@uniza.sk](mailto:pavol.rafajdus@uniza.sk); [vladimir.vavrus@kves.uniza.sk](mailto:vladimir.vavrus@kves.uniza.sk)

G. Scelba  
DIEEI – Universit degli Studi di Catania, Catania (CT), Italy  
e-mail: [giacomo.scelba@dieei.unict.it](mailto:giacomo.scelba@dieei.unict.it)

There are two main approaches for low speed sensorless control of an SRM—Active probing (e.g., [8, 9]) and high frequency injection. Compared to other machines, the use of high frequency approach with the SRM provides additional challenges. Most of these are connected to the square waveform of motoring current, which is composed of a significant amount of higher harmonics. This complicates position signal separation. As was shown in [10], continuous phase excitation can improve the harmonic spectrum at the cost of generating negative torque. Alternatively synchronous frames can be used for current filtering [11]. Another challenge is the usage of asymmetric H-bridge converters that do not enable controlled application of negative voltage to the phase. Therefore a DC bias might be necessary. These issues can be mitigated significantly by using separate sensing coils, but this approach requires additional hardware [12]. Use of advanced algorithms to process information, such as Artificial Neural Networks, is also being investigated [13]. While complex, these methods can account for non-linearities and disturbances that are difficult to implement using classical mathematical modeling.

Differently than [11], the proposed solution extracts the information on the rotor position through a demodulation algorithm using a stationary high frequency sine wave voltage injection. A combination of band-pass and Low-Pass Filters, coordinate transformations, and synchronous frames is used to extract position error information. This position error is used by a Phase Locked Loop (PLL) to calculate rotor speed and position values for the control structure. The delay caused by this algorithm is actively compensated.

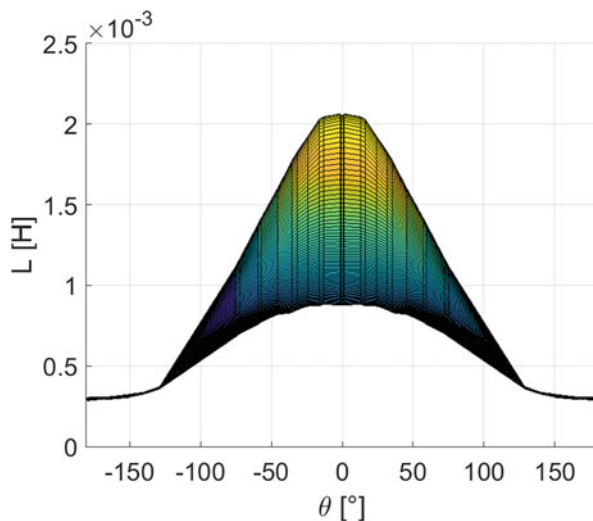
## 2 Switched Reluctance Drive Description

Switched Reluctance Motor Drive (SRMD) used in this study is composed of a 3 phase 18/12 SRM and an asymmetric half-bridge converter. Both the motor and converter were developed at Department of Power Electrical Systems on University of Zilina for a small electric truck. Basic parameters of the machine are shown in Table 1 [14]. Inductance profile is shown in Fig. 1. The converter uses FF400R06KE3 IGBT modules. Sampling frequency is set to 20 kHz.

**Table 1** SRM parameters

Parameter	Value
Nominal voltage	300 V
Nominal phase current (RMS)	22.4 A
Maximum allowed instantaneous phase current amplitude	200 A
Rated power	16 kW
Rated speed	5000 rpm
Rated torque	30 Nm
Maximum static torque	250 Nm

**Fig. 1** Inductance profile of analyzed SRM. Note that peak inductance is saturated from 2.06 to 0.89 mH as the current increases from 0 to 200 A



### 3 Signal Injection

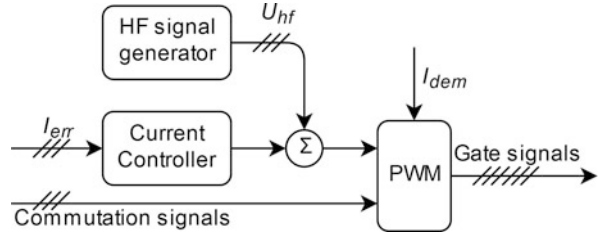
Performance and accuracy of any high frequency voltage sensorless method is based on a correct signal injection. This is especially true in the SRMD for several reasons:

- Square shape of main phase excitation current produces a significant amount of higher harmonics.
- The asymmetric half-bridge converter does not allow injection of negative voltage. Therefore a DC bias is required to inject a harmonic waveform correctly.
- An unipolar switching strategy might be preferred to reduce current ripple and converter losses. However, this approach distorts the waveform shape.
- By injecting into an active phase, the signal gets distorted by inductance saturation. On the other hand, not using the excited phase for injection removes at least one source of information for position estimation.

A 2 kHz stationary field voltage injection was selected for this work. While higher injection frequencies are desirable as they allow easier separation from motoring current harmonics, the selected frequency is a maximum practical value achievable for a 20 kHz switching and sampling frequency. Bipolar switching is used for the injection in unexcited phases and in the active phase when the demanded current is lower than 40 A. To lower current ripple during motoring an unipolar switching scheme is used for the active phase above this current threshold. Certain load dependence can therefore be expected due to inductance saturation.

While this approach can deteriorate accuracy and stability estimation during motoring, it decreases current ripple significantly. Figure 2 shows a block diagram of injection. The PWM block not only calculates correct duty cycle for the converter

**Fig. 2** Block diagram of voltage injection



transistors, but also selects the appropriate switching scheme depending on the demanded current value  $I_{dem}$  and commutation signals.

## 4 Low Speed Sensorless Method

As it was shown in [11], the reverse inductance profile  $1/L$  of a SRM phase can be decomposed by a series of cosine terms. In the following study the reciprocal value of the inductances is represented by approximating it with a DC term plus a cosinusoidal term. Used  $1/L$  waveform equations for each phase are shown in (1)–(3).

$$\frac{1}{L_a} = A + B \cdot \cos(\omega_r t) \quad (1)$$

$$\frac{1}{L_b} = A + B \cdot \cos\left(\omega_r t - \frac{2\pi}{3}\right) \quad (2)$$

$$\frac{1}{L_c} = A + B \cdot \cos\left(\omega_r t - \frac{4\pi}{3}\right) \quad (3)$$

Constants “A” and “B” represent the inductance profile constants. As will be shown later in this paper, their exact value is irrelevant for this analysis. A stationary voltage (4) is injected into all phases. By neglecting the voltage drop in stator resistance and using a Band-Pass Filter, the resulting current response to the injection can be calculated according to (5)–(7). For better clarity during principle explanation, these equations assume that all current components related to motoring current have been filtered out.

$$U_{hf} = U_{amp} \cdot \sin(\omega_{hf} t) \quad (4)$$

$$i_{aBPF} = \frac{U_{amp}}{\omega_{hf}} \left\{ A \cdot \sin(\omega_{hf} t) + \frac{1}{2} B \cdot \sin \cdot [((\omega_{hf} + \omega_r) t) + ((\omega_{hf} - \omega_r) t)] \right\} \quad (5)$$

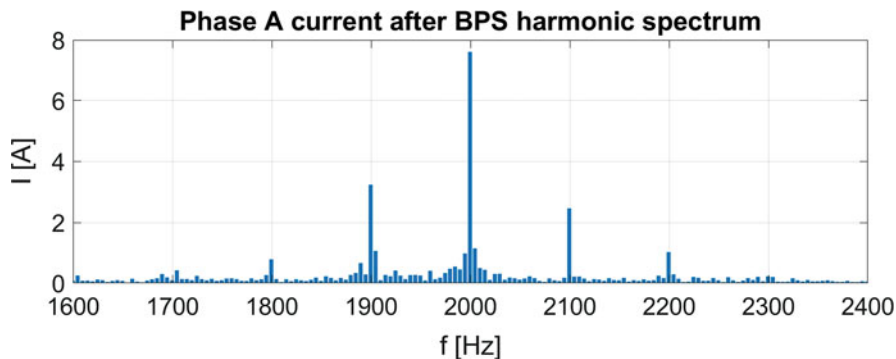


Fig. 3 Harmonic spectrum of the filtered motor phase A

$$i_{bBPF} = \frac{U_{amp}}{\omega_{hf}} \left\{ A \cdot \sin(\omega_{hf}t) + \frac{1}{2} B \sin \left[ \left( (\omega_{hf} + \omega_r) t - \frac{2\pi}{3} \right) + \left( (\omega_{hf} - \omega_r) t + \frac{2\pi}{3} \right) \right] \right\} \quad (6)$$

$$i_{cBPF} = \frac{U_{amp}}{\omega_{hf}} \left\{ A \cdot \sin(\omega_{hf}t) + \frac{1}{2} B \sin \left[ \left( (\omega_{hf} + \omega_r) t - \frac{4\pi}{3} \right) + \left( (\omega_{hf} - \omega_r) t + \frac{4\pi}{3} \right) \right] \right\} \quad (7)$$

As it can be seen in the high frequency current responses, three harmonic waveforms are expected to be present in the harmonic spectrum as a result of the high frequency voltage injection. Two of these waveforms, which contain rotor position information, form sidebands in respect to the main injected frequency. This can clearly be seen in harmonic spectrum shown in Fig. 3, which was captured from a simulation. The simulation will be described later. The rotor speed of 520 rpm corresponds to a frequency of 104 Hz. Sidebands containing double of the rotor position can also be seen in this figure, but they are suppressed by the demodulation algorithm. To improve figure clarity during principle explanation, no-load conditions were selected as they are not distorted by interference from the motoring current.

Because the studied machine has three phases a regular Clarke transformation (8) can be used to obtain currents in the orthogonal stationary frame. As can be seen in (9) and Fig. 4, the main high frequency current response is canceled out in this transformation.

$$i_{\alpha\beta} = \begin{bmatrix} 1 & -\frac{1}{2} & -\frac{1}{2} \\ 0 & +\frac{\sqrt{3}}{2} & -\frac{\sqrt{3}}{2} \end{bmatrix} \begin{bmatrix} i_a \\ i_b \\ i_c \end{bmatrix} \quad (8)$$

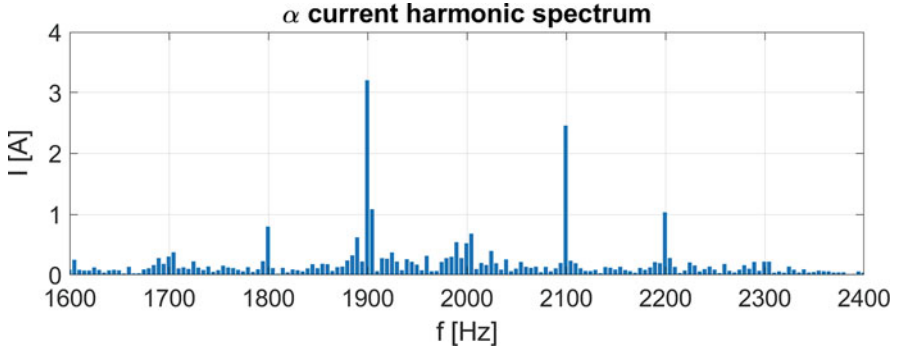


Fig. 4 Harmonic spectrum of  $\alpha$  current component

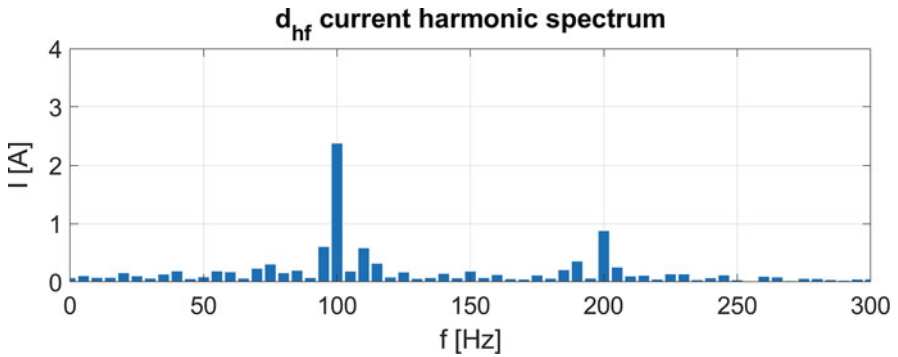


Fig. 5 Harmonic spectrum of  $d_{hf}$  current component

$$i_{\alpha\beta} = \frac{U_{amp}}{\omega_{hf}} \left[ \frac{3}{4} B \cdot \left( e^{j\frac{\pi}{2} - j(\omega_{hf} - \omega_r)t} + e^{j\frac{\pi}{2} - j(\omega_{hf} + \omega_r)t} \right) \right] \quad (9)$$

To further simplify the equations an amplitude of remaining high frequency current response is defined in (10).

$$I = \frac{3}{4} B \cdot \frac{U_{amp}}{\omega_{hf}} \quad (10)$$

A further reference frame transformation, which is synchronous to the injected high frequency, is exploited next in (11). As it can be seen in Fig. 5 the 104 Hz rotor information is easily distinguishable.

$$i_{dqhf} = i_{\alpha\beta} \cdot e^{j\omega_{hf}t} = I \left[ e^{j(\frac{\pi}{2} + \omega_r t)} + e^{j(\frac{\pi}{2} - \omega_r t)} \right] \quad (11)$$

Another step rotates the signal using estimated rotor speed  $\hat{\omega}_r$  from the last known step according to (12). The first of the two remaining terms is  $\hat{\omega}_r + \omega_r$ .

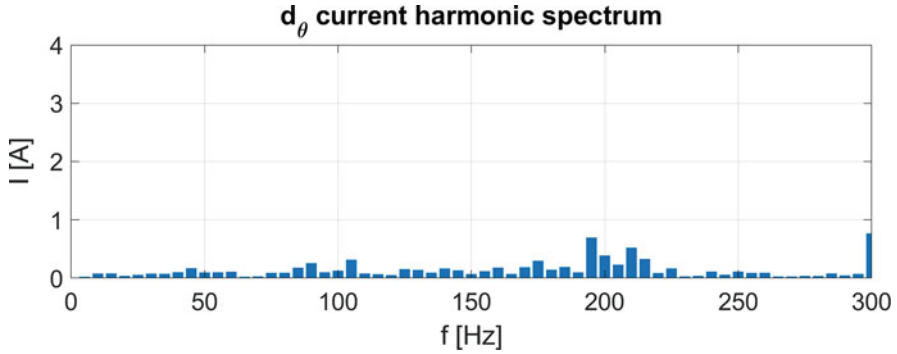


Fig. 6 Harmonic spectrum of  $d_{\theta}$  current component

Assuming correct estimation this term rotates with double of the actual rotor speed. Above certain speed the following Low-Pass Filter mitigates this term. It can be seen in Fig. 5 as a small amplitude at a frequency of 208 Hz. The second term  $\hat{\omega}_r - \omega_r$  is effectively a direct representation of position error. Decreasing cut-off frequency of the Low-Pass Filter limits impact of the first term, but also limits the dynamics of the entire structure because the position error cannot be higher than this cut-off frequency (13) (Fig. 6).

$$i_{dq\theta} = i_{dqhf} \cdot e^{j(-\frac{\pi}{2} + \hat{\omega}_r t)} = I \left[ e^{j(\hat{\omega}_r + \omega_r)t} + e^{j(\hat{\omega}_r - \omega_r)t} \right] \quad (12)$$

$$i_{dqLPF} = LPF(i_{dq\theta}) = I e^{j(\hat{\omega}_r - \omega_r)t} \quad (13)$$

Using both  $d$  and  $q$  components to extract the position error information according to (16) effectively cancels the amplitude represented by  $I$  introduced in (10). Therefore this method is dependent only on the inductance waveform shape and not its absolute values. Of course, the signal has to have a high enough Signal to Noise Ratio to be processed correctly.

$$\theta_{err} = (\omega_r - \hat{\omega}_r)t = \theta_r - \hat{\theta}_r \quad (14)$$

$$i_{dqLPF} = I e^{j(-\theta_{err})} \quad (15)$$

$$\theta_{err} = -\text{atan2}(i_{dLPF}, i_{qLPF}) \quad (16)$$

The High Frequency Demodulator (HFD) is shown in Fig. 7.

A Phase Locked Loop (PLL) is used to estimate speed and position based on the position error information provided by the HFD. Speed output is connected to the speed controller. Position information is used not only for the commutation control, but also for the reference frame transformation (12) in the HFD. Note that the position for the commutation control is compensated for the processing delay.

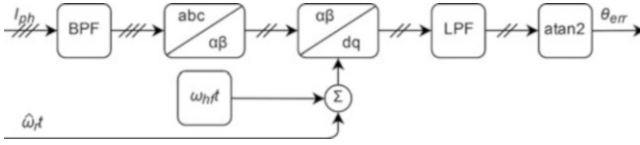


**Fig. 7** Block diagram of High Frequency observer

**Fig. 8** Block diagram of the proposed method

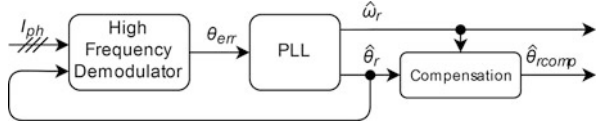
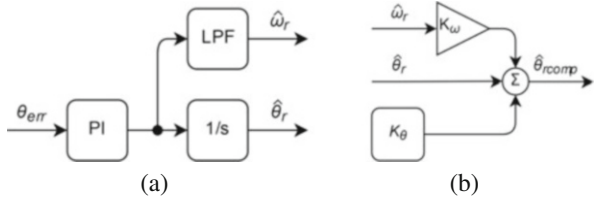


**Fig. 9** Block diagrams of Phased Locked Loop and Compensation block. (a) Phase Locked Loop. (b) Compensation block



The compensated position is not used for the HFD as it would introduce interference with the internal dynamics of the demodulator (Fig. 8).

The PLL consists of a PI controller, an integrator, and another Low-Pass Filter, which is connected according to Fig. 9a. Compensation block, shown in Fig. 9b, corrects errors made by the delay in signal processing. This includes not only the calculation time itself, but also the phase delay caused by the multiple filters used in the algorithm. It consists of two parts. Firstly the static delay is compensated by adding a constant to the estimated position. Secondly a compensation of delay for the given speed is added. As the delay of position calculation is a linear function of speed a simple multiplication of estimated speed and an appropriate constant is sufficient. Estimation delay due to acceleration is not added because it would require speed difference information, which can be affected significantly by noise. Also if the SRMD dynamic is high, increasing the bandwidth of PLL PI controller can effectively reduce this particular estimation delay.

## 5 Performance Evaluation

### 5.1 Modeling of the SRM Drive

Block diagram of simulation implemented in Simulink is shown in Fig. 10. It is composed from the SRM itself, an accurate converter model (using models of actual IGBTs) created with Simscape Power Systems toolbox, speed controller, current controllers, phase commutation control, and the proposed method estimation block.



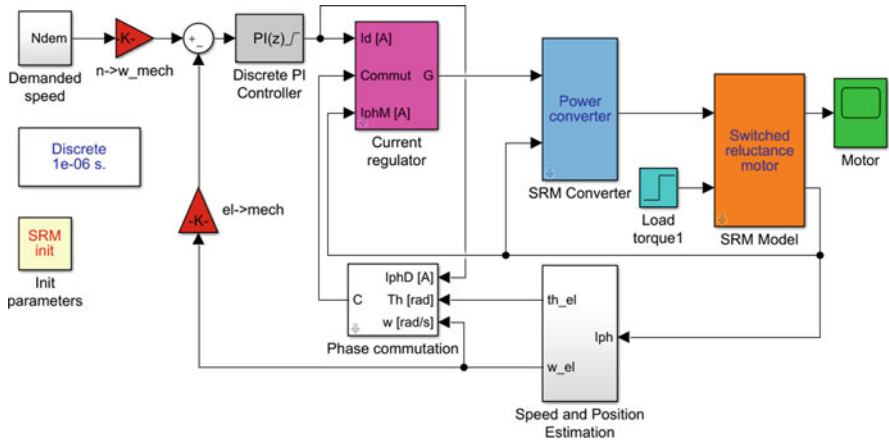


Fig. 10 Sensorless SRMD implementation in Simulink

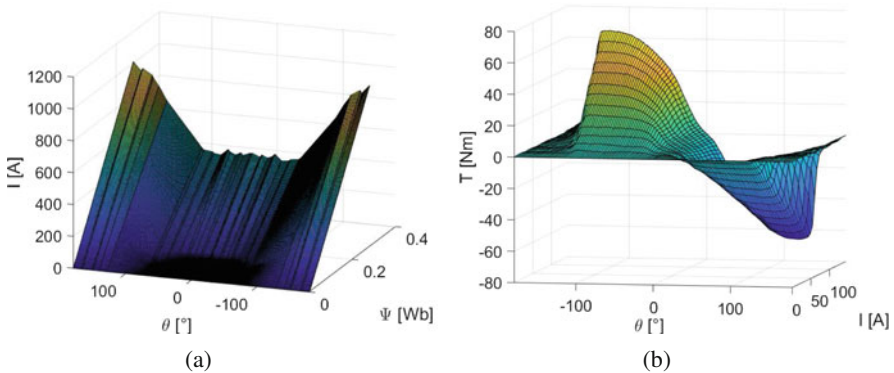


Fig. 11 Parameter maps used in analysis. (a) Reverse flux-linkage map. (b) Torque map

During the entire simulation the control algorithm uses only estimated speed and position. While the simulation runs at a step of  $1 \mu\text{s}$ , the control and sensorless blocks are set to  $50 \mu\text{s}$  according to the 20 kHz sampling frequency of the actual drive.

The SRM model is based on a reverse flux-linkage map  $i = f(\theta, \Psi)$  and the torque map  $T_e = f(\theta, i)$  [14], which are shown in Fig. 11a, b.

### 5.2 Simulation Results

As can be seen in Fig. 12, the simulation run consists of five distinct parts:

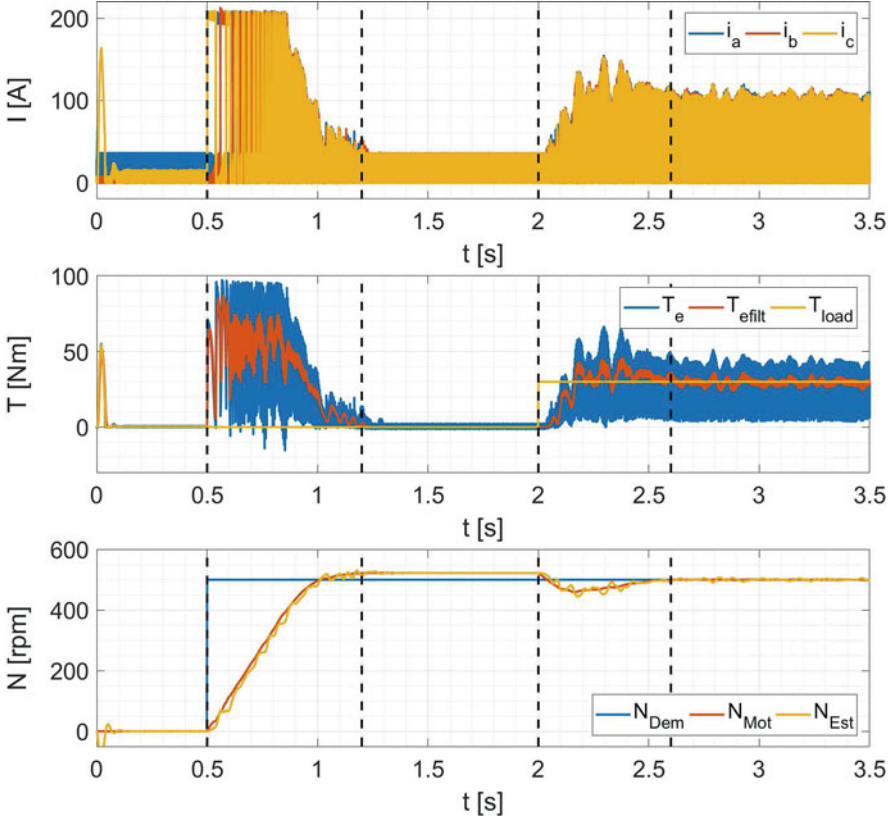


**Fig. 12** Phase currents (top), torques (middle) and speed (bottom) of the SRMD operation using only estimated values

- $t \in (0; 0.5)$ —Demanded speed is set to zero and rotor position is deliberately set to  $180^\circ$ . The rotor is braked in this position and cannot move. This simulates the worst case of an unknown starting position.
- $t \in (0.5; 1.2)$ —A speed of 500 rpm (10% of nominal speed) is demanded with zero load torque. Because of this and the control structure dynamics, the speed overshoots slightly to approximately 520 rpm.
- $t \in (1.2; 2)$ —Demanded current is zero because of the overshoot and no load torque.
- $t \in (2; 2.6)$ —A step change of load torque to nominal value of 30 Nm is applied to demonstrate robustness of the algorithm. It should be noted that this sudden loading is not expected in a traction application.
- $t \in (2.6; 3.5)$ —This last interval shows steady state accuracy under nominal load.

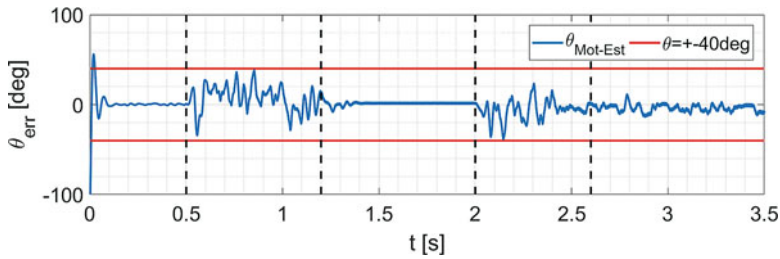


**Fig. 13** Electrical position estimation error during the simulation

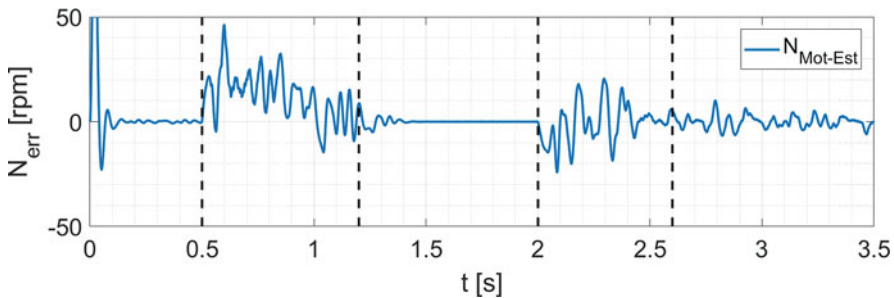


**Fig. 14** Speed error during the simulation

Electrical position error is shown in Fig. 13. The red boundary marks the  $\pm 40^\circ$  of error, or  $3.33^\circ$  mechanical. If the rotor position stays within these limits, torque generation capability should not be reduced by more than 25%. This is acceptable for a low speed and low load operation and is comparable to [10]. The algorithm correctly converges to the starting rotor position within a very short period. During the acceleration to demanded speed, the position accuracy is negatively affected by interference from the motoring current, but stays within the acceptable limits. The no-load interval again reaches very good accuracy and stability due to the lack of motoring currents. During the load torque step change transient, the position error is again increased. It can be seen that during stable nominal load operation, the position error ripple is higher than during no load and also the mean value of position error is not zero. However, the error is still within specified limits.

Speed error, recalculated to rpm, is shown in Fig. 14. In regions without motoring current, the error is negligible, similarly to position error. In the presence of motoring current there is a noticeable ripple even with the Low-Pass Filter in the PLL. Design of speed controller must account for this ripple. During the initial transient to correct position, the negative estimated speed might cause the speed controller to apply motoring current, causing the rotor to move if adequate braking is not applied.

It must be noted that the high torque ripple seen in Fig. 12 is not caused only by the position error, but also by the requirement to use only one phase for motoring at any given moment. Because the studied SRM is a 3 phase machine, this causes severe ripple. The filtered torque values stay high, verifying correct estimation.

## 6 Conclusions

A new approach for the estimation of position and speed of a Switched Reluctance Motor Drive based on stationary high frequency voltage injection was shown. This method improves signal processing, which separates the necessary information from the measured current signal. The principle was described thoroughly and verified by a simulation using an accurate model of the motor and converter.

Using both bipolar and unipolar switching scheme under appropriate conditions significantly reduces current ripple and improves converter efficiency. The peak injected current reaches values up to 35 A (corresponding to 17.5% of allowed instantaneous current amplitude), but given the SRM characteristics the resulting negative torque is negligible. The inductance saturation at this current level is also not significant, but during motoring section of the period. It was shown that even during high-power motoring the accuracy, decreased by inductance saturation from motoring current, is still within required limits. High amplitude of injected voltage is also permissible, as this method is considered for low speed operation, where there is sufficient supply voltage available compared to the Back EMF.

Simulation results show that the method is capable of correct startup from an unknown position to at least 10% of the nominal speed of the machine and sustain this speed both in no-load and nominal load conditions. Robustness of the algorithm was verified by the acceleration to speed and load torque step change transients. Experimental verification will be published in a following paper.

**Acknowledgements** This work was supported by VEGA 1/0774/18 and by ITMS: 26210120021.

## References

1. T.J.E. Miller (ed.), *Electronic Control of Switched Reluctance Machines*. Newnes Power Engineering (Reed Educational and Professional Publishing Ltd., London, 2001). ISBN: 0-7506-50737
2. M. Cacciato et al., A switched reluctance motor drive for home appliances with high power factor capability, in *2008 IEEE Power Electronics Specialists Conference*, June 2008, pp. 1235–1241
3. N. Sakr et al., A combined switched reluctance motor drive and battery charger for electric vehicles, in *IECON 2015 - 41st Annual Conference of the IEEE Industrial Electronics Society*, November 2015, pp. 001770–001775. <https://doi.org/10.1109/IECON.2015.7392357>
4. A. Peniak, J. Makarovic, P. Rafajdus, Replacing of DC motor in the first Slovak electric car by an optimized switched reluctance motor, in *2016 ELEKTRO*, May 2016, pp. 350–354

5. M.S. Islam et al., Design and performance analysis of sliding-mode observers for sensorless operation of switched reluctance motors. *IEEE Trans. Control Syst. Technol.* **11**(3), 383–389 (2003). ISSN: 1063-6536
6. Y. Saadi et al., Sensorless control of switched reluctance motor with unknown load torque for EV application using extended Kalman filter and second order sliding mode observer, in *2018 IEEE International Conference on Industrial Technology (ICIT)*, February 2018, pp. 522–528
7. P. Brandstetter, O. Petrtyl, J. Hajovsky, Luenberger observer application in control of switched reluctance motor, in *2016 17th International Scientific Conference on Electric Power Engineering (EPE)*, May 2016, pp. 1–5
8. J. Bekiesch et al., A simple excitation position detection method for sensorless SRM drive, in *2007 European Conference on Power Electronics and Applications*, September 2007, pp. 1–8
9. A. Sarr et al., Sensorless control of switched reluctance machine, in *IECON 2016 - 42nd Annual Conference of the IEEE Industrial Electronics Society*, October 2016, pp. 6693–6698
10. E. Kayikci, M.C. Harke, R.D. Lorenz, Load invariant sensorless control of a SRM drive using high frequency signal injection, in *Conference Record of the 2004 IEEE Industry Applications Conference, 2004. 39th IAS Annual Meeting*, vol. 3, October 2004, pp. 1632–1637
11. R. Hu et al., Sensorless control of switched reluctance motors based on high frequency signal injection, in *17th International Conference on Electrical Machines and Systems (ICEMS)*, October 2014, pp. 3558–3563
12. S.M. Ahmed, P.W. Lefley, A new simplified sensorless control method for a single phase SR motor using HF signal injection, in *2007 42nd International Universities Power Engineering Conference*, September 2007, pp. 1075–1078
13. P. Kappes, I. Krueger, G. Griepentrog, Self-sensing method for a switched reluctance motor using delta-sigma modulators and neural networks, in *2017 IEEE International Symposium on Sensorless Control for Electrical Drives (SLED)*, September 2017, pp. 55–60
14. P. Sovicka et al., Current controller with slope compensation for a switched reluctance motor, in *2018 ELEKTRO*, May 2018, pp. 1–6